Experimental Investigation of the Rising Behavior of CO_2 Droplets in Seawater under Hydrate-Forming Conditions

NIKOLAUS K. BIGALKE,*,† GREGOR REHDER,‡ AND GISELHER GUST§

Leibniz Institute of Marine Sciences at the University of Kiel, Wischhofstrasse 1-3, 24148 Kiel, Germany

Received January 23, 2008. Revised manuscript received April 8, 2008. Accepted April 11, 2008.

In a laboratory-based test series, seven experiments along a simulated Pacific hydrotherm at 152°W, 40°N were carried out to measure the rise velocities of liquefied CO_2 droplets under (clathrate) hydrate forming conditions. The impact of a hydrate skin on the rising behavior was investigated by comparing the results with those from outside the field of hydrate stability at matching buoyancy. A thermostatted high-pressure tank was used to establish conditions along the natural oceanic hydrotherm. Under *P*-/*T*-conditions allowing hydrate formation, the majority of the droplets quickly developed a skin of CO_2 hydrate upon contact with seawater. Rise rates of these droplets support the parametrization by Chen et al. (*Tellus* **2003**, *55B*, 723−730), which is based on empirical equations developed to match momentum of hydrate covered, deformed droplets. Our data do not support other parametrizations recently suggested in the literature. In the experiments from 5.7 MPa, 4.8 °C to 11.9 MPa, 2.8 °C positive and negative deviations from predicted rise rates occurred, which we propose were caused by lacking hydrate formation and reflect intact droplet surface mobility and droplet shape oscillations, respectively. This interpretation is supported by rise rates measured at *P*-/*T*-conditions outside the hydrate stability field at the same liquid CO_2-seawater density difference ($\Delta\rho$) matching the rise rates of the deviating data within the stability field. The results also show that droplets without a hydrate skin ascend up to 50% faster than equally buoyant droplets with a hydrate skin. This feature has a significant impact on the vertical pattern of dissolution of liquid CO_2 released into the ocean. The experiments and data presented considerably reduce the uncertainty of the parametrization of CO_2 droplet rise velocity, which in the past emerged partly from their scarcity and contradictions in constraints of earlier experiments.

1. Introduction

With the demand of energy from fossil fuels expected to rise throughout the first half of this century at least, stabilization of atmospheric CO_2 concentrations at levels of 450−750 ppmv requires prevention of CO_2 emissions into the atmosphere in the order of 10^2 to 10^3 Gt of CO_2 within this century (*2*). To meet this requirement, ocean storage of fossil fuel derived CO_2 is being considered among other carbon capture and storage (CCS) strategies (*2*). Results of the following study address scenarios of liquid CO_2 release into the water column at depths between the CO_2/seawater density inversion and the CO_2 liquid/gas phase boundary (Figure 1). Liquid CO_2 release might occur either intentionally by direct injection into the water column or by accidental seepage from subsedimentarily stored CO_2. Figure 1 shows that for the depth range under consideration the *P*-/*T*-conditions generally allow hydrate formation. Several investigators have observed that hydrate readily crystallizes at the interface between liquid CO_2 and seawater to form skins around the droplets (e.g., *3–8*). The low density liquid creates plumes of ascending droplets with CO_2 dissolving into the surrounding seawater (*9*). Among the factors influencing the vertical distribution of dissolved CO_2 is the droplet's terminal rise velocity, u_T. u_T has been modeled using a variety of approaches in several publications (e.g., *1, 7–11*). However, experimental data on the behavior of CO_2 under controlled thermodynamic conditions is scarce. Observations made in a field experiment (*4*) have been used repeatedly as a reference for model calculations of u_T. Brewer et al. (*4*) used a simplified buoyancy equation adopted from Holder et al. (*7*) to match the observed velocities. Zhang (*11*) pointed out that this equation cannot be employed in general and used a function approximating the standard drag curve of a rigid sphere instead. This had been common practice in other works (e.g., (*8*)) in which droplets were assumed to behave

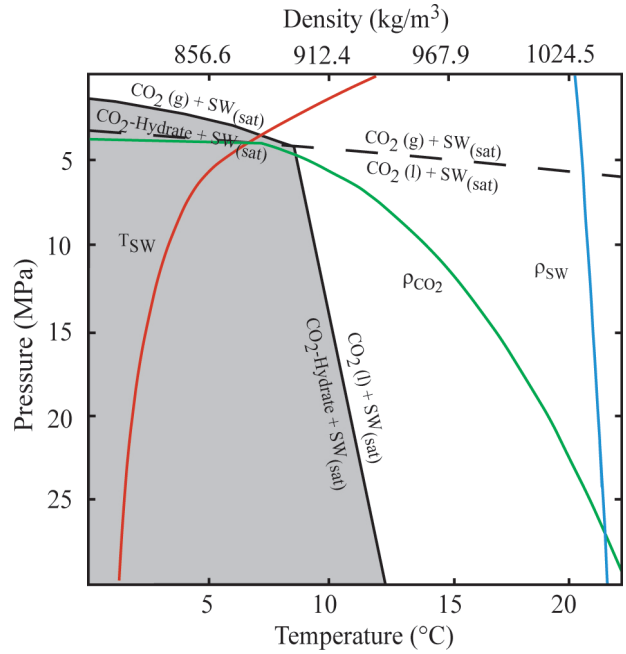

FIGURE 1. Phase diagram of CO_2 and seawater. The gray area marks the stability field of CO_2 clathrate hydrate. Also shown is the gas/liquid phase transition (dashed line) for pure CO_2. The red line denotes a depth−temperature profile of the Pacific Ocean at 152°W, 40°N (WoceCTD station no. 6819) (*23*). Green and blue lines denote densities of CO_2 and seawater (35.0 PSU), respectively at *P*-/*T*-conditions given by the hydrotherm. Phase boundaries calculated after Sloan (*16*); seawater and CO_2 densities calculated after Siedler and Peters (*24*) and Angus et al. (*25*), respectively.

* Corresponding author e-mail: nbigalke@ifm-geomar.de; phone: +49-431-600-1410; fax: +49-431-600-1400.
† Leibniz Institute of Marine Sciences at the University of Kiel.
‡ Baltic Sea Research Institute Warnemuende, Seestr. 15, 18119 Rostock-Warnemünde, Germany.
§ Technical University Hamburg-Harburg, Department of Ocean Engineering, Schwarzenbergstr. 95, 21073 Hamburg, Germany.

10.1021/es800228j CCC: $40.75
Published on Web 06/11/2008

TABLE 1. Experimental *P*-/*T*-Conditions and Corresponding Liquid Densities[a]

P [MPa]	*T* [°C]	$\rho(CO_2)$ [kg/m³]	ρ(SW) [kg/m³]	$\Delta\rho$ [kg/m³]	P_{eq} [MPa]	Morton number
5.7	4.8	915.1	1030.3	115.2	2.6	5.9×10^{-10}
8.3	3.6	943.9	1031.7	87.8	2.2	5.1×10^{-10}
9.9	3.2	957.0	1032.4	75.4	2.1	4.6×10^{-10}
11.9	2.8	971.1	1033.4	62.3	2.0	4.0×10^{-10}
14.7	2.5	987.2	1034.7	47.5	1.9	3.1×10^{-10}
17.5	2.0	1002.4	1036.1	33.7	1.8	2.3×10^{-10}
20.2	1.9	1014.1	1037.3	23.2	1.8	1.6×10^{-10}
18.3	13.1	958.8	1034.2	75.4	40.5	1.5×10^{-10}
22.0	13.9	974.0	1036.3	62.3	48.9	1.1×10^{-10}
24.8	13.1	989.5	1037.0	47.5	40.5	9.2×10^{-11}

[a] Conditions of experiments run outside the hydrate stability field are listed in the bottom three rows. Calculations of seawater and CO_2 densities after Siedler and Peters (*24*) and Angus et al. (*25*), respectively. Three-phase equilibrium pressures (P_{eq}) calculated for experimental temperatures after Sloan (*16*). Mo = $g\mu_{SW}^4\Delta\rho/(\rho_{SW}^2\sigma^3)$ where μ_{SW} is the dynamic viscosity of seawater (*24*) and $\sigma = 0.023$ kg/s².

as rigid spheres upon formation of hydrate skins. It was shown by Ozaki et al. (*5*) that deformation of hydrate-coated droplets does occur and this and follow-up studies (*1, 10*) demonstrate that rise velocities can be overestimated using the rigid sphere theory. Gangstø et al. (*10*) applied a model based on experiments with air bubbles and a variety of liquids under atmospheric pressure (*12*). Four out of five observational points reported in ref (*4*) were well matched; however, due to the limited depth range of the experiments, potential perturbations, and scarcity of observational points, the validity of this parameterization is uncertain. Furthermore, the model needs to be expanded in order to be valid for systems with a liquid (rather than gas) as dispersed phase. Chen et al. (*1*) developed a semiempirical parameterization of the rise velocity to successfully match observations made in tank experiments (*5*) at three different *P*-/*T*-conditions; however, these were outside typical oceanic conditions. Considerable differences exist in both the experimental data as well as the different model parametrizations. This study addresses this inconsistency by presenting a comprehensive set of rise rates of CO_2 droplets at *P*-/*T*-conditions simulating oceanic conditions within the hydrate stability field as well as at conditions outside the field of hydrate stability. The data are used to re-evaluate the different parametrizations of u_T suggested in the literature.

2. Experimental Section

Necessary *P*-/*T*-conditions for hydrate formation were realized in a pressure laboratory designed to simulate marine conditions at depths of up to 5500 mbsl. The central part of the facility is a stainless steel autoclave measuring 1.4 m inner height and 0.3 m inner diameter. The vessel was filled with tap water to convey temperature and hydrostatic pressure to the inner assembly selected for the experiments. Details of the pressure laboratory are presented in Rehder et al. (*13*). The inner assembly, its mode of operation, and the experimental setup are described in Section A1 of the Supporting Information.

The experiments took place in stagnant synthetic seawater of 35 PSU. *P*-/*T*-conditions were selected to match discrete depths along a marine hydrotherm of the Pacific Ocean at 152°W, 40°N (Figure 1, Table 1). Seven data sets were gathered within the field of hydrate stability. Three additional data sets outside the field of hydrate stability were collected. To assess the effect of hydrate skin formation on the rise velocity, *P* and *T* in the additional experiments were set to values to match density differences ($\Delta\rho$) between CO_2 and seawater (and thus buoyancy forces) of three experiments from within the field of hydrate stability. An overview of the experimental conditions is given in Table 1. Droplet rise rates and sizes were determined optically by means of two low-resolution cameras fixed at a vertical distance of 34 cm from each other next to the rising chamber inside and one high-resolution camcorder filming from outside of the pressure vessel, respectively. In the images recorded, droplets appeared as dark ellipses. Their sizes were expressed by the equivalent radius, r_e, which is defined by

$$r_e = (a^2 b)^{1/3} \quad (1)$$

with a and b being major and minor semiaxis of the ellipse, respectively. Section A2 of the Supporting Information details the analysis of the high-resolution video material.

3. Results and Discussion

3.1. Droplet Shape and Motion Characteristics. In our experiments, droplet radii varied from 0.6 to 15.0 mm, with droplet shapes shifting from spherical at small radii via regular-ellipsoidal at intermediate to irregularly deformed ellipsoids at large radii. Figure 2 shows the relationship between equivalent radius r_e and aspect ratio of droplets rising inside and outside of the hydrate stability field. The aspect ratio is defined as the ratio of major and minor axes of the best fitting ellipse to the droplets. Most figures show an inflection at a droplet radius around 2 mm. The slope of the aspect ratio from 2 mm onward varies with ambient pressure and temperature. There is a trend toward stronger flattening at shallower simulated seawater depth. Accordingly, the smallest change of the aspect ratio throughout the whole range of droplet radii is observable at highest pressures within the hydrate stability field, at 20.2 MPa and 1.9 °C (Figure 2a). Increased scatter is observed in the data sets from experiments outside the hydrate stability field.

Droplet shapes can be described in terms of the relevant Morton and Eötvös numbers (*14*). At Morton numbers in the range of this study (Table 1) the shape of a droplet can be sufficiently characterized by the Eötvös number alone, which is proportional to buoyancy forces divided by interfacial tension forces (*14*). There seems to be no systematic investigation of the interfacial tension σ of CO_2 droplets in seawater at *P*-/*T*-conditions in the range of interest in the literature. Ohmura et al. (*15*) estimate σ_{CO_2}/seawater at a seawater depth of 3300 m to be 24 g/s² while Gangstø et al. (*10*) set σ_{CO_2}/seawater to the constant value of 23 g/s² for the range of seawater depths from 496.8 to 804.5 mbsl. We assume σ_{CO_2}/seawater to be constant within the *P*-/*T*-range of our experiments. Droplet buoyancy is proportional to the volume of the droplet and the density difference between CO_2 and seawater. Lower buoyancy toward small diameters or high simulated seawater depths shifts droplets to more spherical shapes. Larger droplets and those released at shallower seawater depths have greater buoyancy and consequently are deformed toward ellipsoidal shapes. Droplets rising at conditions satisfying hydrate formation show less deformation than those released outside of the hydrate stability field (Figure 2b−d). This indicates that hydrate skins counter the deformation of droplets, which is in accordance with findings from field (*4*) and laboratory experiments (*6*).

Oscillations were predominantly observed at *P*-/*T*-conditions outside the field of hydrate stability. In general, the onset of shape oscillations coincides with vortex shedding from the wake of the droplets (*14*). Reynolds numbers, Re, at which vortex shedding sets in are often referred to as "lower critical Reynolds numbers", Re_{crit}. Outside of the hydrate stability field, shape oscillations set in at $r_e = 3.1$ mm (Re =

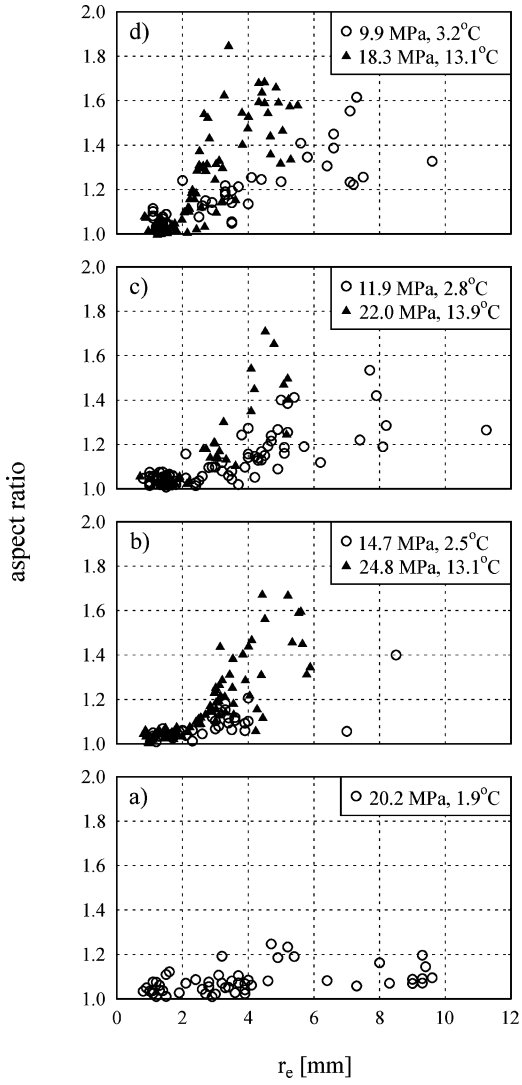

FIGURE 2. Aspect ratio, defined as the ratio of major and minor axis of droplets. Open circles and black triangles represent droplets released inside and outside of the hydrate stability field, respectively. More data are available in Section A3 of the Supporting Information.

670) at 17.9 MPa, 13.1 °C; $r_e = 3.5$ mm (Re = 710) at 23.2 MPa, 13.9 °C; and at $r_e = 3.8$ mm (Re = 760) at 24.3 MPa, 13.1 °C.

Within the hydrate stability field oscillations were mostly suppressed. This suggests the formation of a rigid hydrate skin around the droplets. In our experiments, occasional oscillations were observed at conditions close to the phase boundary (from 5.7 MPa, 5.0 °C to 11.9 MPa, 2.8 °C). In some of these instances, droplets were seen to develop a hydrate skin only after they had come to rest under the lid of the rising tube (Figure 3). This indicates that significant hydrate formation did not occur before these droplets detached from the nozzle and had risen about 100 cm through the tube, even though the *P*-/*T*-conditions were inside the hydrate stability field. In contrast, no oscillations were observed in experiments conducted at pressures higher than 14.7 MPa nor at advanced stages of the experiments. This indicates that at these conditions hydrate crystallization around droplets was significantly faster. The probability of a hydrate nucleus to reach a critical size that ensures thermodynamic stability and allows further growth is dependent on the concentration of the dissolved hydrate-forming gas species in the bulk fluid and the degree of supercooling (i.e., the distance in the *P*-/*T*-diagram from the 3-phase boundary) (*16*). Nucleation is considerably facilitated by the presence of foreign bodies serving as seed crystals (e.g., microscopic dust particles) or water microstructures which have been preserved in water that has been in contact with hydrates before (*16, 17*). For methane bubbles released within the methane hydrate stability field in an open ocean experiment, it has been shown that already established shape oscillations were suppressed after hydrate formed at the interface, which could take several minutes from the time of release (i.e., several 10s of meters of rise) (*18*). Our data clearly show that immediate formation of hydrate at the CO_2−seawater interface cannot be assumed for droplets released in undersaturated waters under *P*-/*T*-conditions not too far from the three-phase boundary.

A considerable part of the scatter in the records of droplet flatness can be attributed to droplets without a hydrate skin, allowing shape oscillations at Re > Re_{crit}. This is evident in Figure 2 by comparing the increased scatter of data from outside the hydrate stability field relative to the low scatter of the experiment farthest within the hydrate stability field, where immediate hydrate skin formation is furthermore evident from the high sphericity of the droplets throughout the entire radius range.

3.2. Rise Velocity. All data on terminal velocities measured inside the CO_2 hydrate stability field are shown in Figure 4. The general trends show the expected increase in u_T with droplet radius for small radii, and a decrease of u_T with increasing simulated seawater depth. Terminal velocities increased to a radius of maximum velocity and slightly decreased with further increase of r_e. The general trend of the data sets is in accordance with the data presented by Ozaki et al. (*5*). Deviations are detectable in the four data sets obtained at conditions from close to the phase boundary up to 11.9 MPa, 2.8 °C (Figure 4a−d). While data points at $r_e \geq 4$ mm show a diffuse scatter, the deviations of smaller droplets appear to be systematic (Figure 4a and d). The rise rates of these small-sized outliers exceed those following the general trend by up to 50%.

The terminal rise velocity u_T of the droplets can be derived by balancing buoyant and drag forces and reads

$$u_T = [(8gr(\rho_{SW} - \rho_{Co_2}))/(3C_{d\rho})]^{0.5} \quad (2)$$

where g is gravitational acceleration, r is droplet radius, ρ_{SW} and ρ_{CO_2} are seawater and CO_2 density, respectively, and C_d is the drag coefficient. The main uncertainty is related to the prediction of C_d. For rigid, spherical, and steadily moving particles, C_d can be correlated with Re using standard drag curves (*14*). While rise rates calculated on grounds of standard drag curves may be correct for spherical droplets with a rigid interface they will deviate from observed rise rates for flattened, oscillating droplets with a mobile interface.

Deformation Effects. Droplet deformation to ellipsoidal shapes results in an increased flow resistance since the cross section perpendicular to the direction of motion increases. Effects arising from droplet deformation are evidenced by comparing our observations to the rise rates calculated according to Zhang (*11*) who proposed a rigid sphere approach (Figure 4). While there is good agreement in the spherical size regime, the limitations of the approach are clearly demonstrated by the negative deviations of observed rise rates from calculations as droplets deform to ellipsoid shapes.

Effect of Surface Mobility. A mobile surface significantly keeps the velocity gradient and thus friction at the interface of the fluid particle at a minimum and thus allows high rise velocities (*14*). A theory of the effect of hydrate skin formation on surface mobility has been proposed for methane bubbles by McGinnis et al. (*19*) and is essentially adopted here: Hydrate that crystallizes at the surface of the droplet is swept to the south pole of the droplet and accumulates there to form a hydrate skin. As the skin grows upward along the

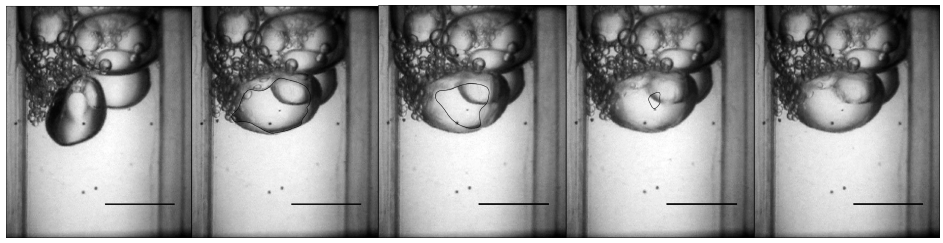

FIGURE 3. Lateral spreading of a hydrate skin around a droplet trapped under previously ascending droplets now clogging the conduit. Length scale at bottom right of each image is 10 mm, entire sequence duration is 3.4 s.

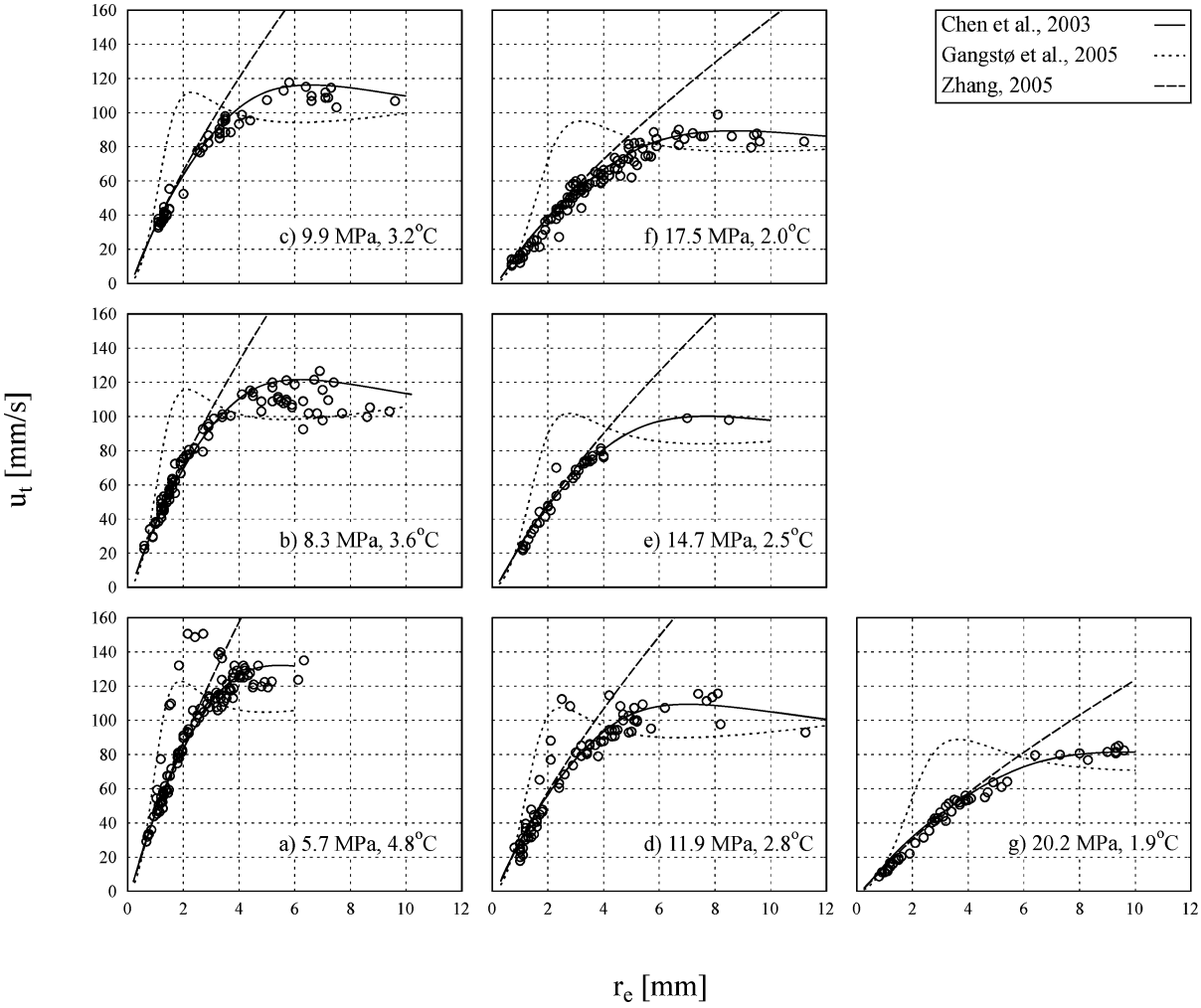

FIGURE 4. Terminal velocities of droplets rising at hydrate forming conditions. Circles represent observed velocities of individual droplets, lines denote calculated values according to drag parametrizations found in refs *1, 10, 11* as indicated in the key.

interface, surface mobility of the droplet decreases and friction increases. Friction reaches a maximum when the entire droplet is coated by hydrate. Consequently, different parameterizations of droplet rise velocities for "clean" (i.e., mobile surface) and hydrate coated (immobile surface) droplets are required. Surface immobilization can also be caused by surface active contaminations (surfactants) in the continuous medium. Retardation of the interface mobility by surfactants is a result from tangential stress caused by local reductions of the surface tension (*14, 20*). Surface mobility can only be realized if effects arising from contaminations are negligible. While even minute contamination can have a major impact on the drag of gaseous bubbles in aqueous systems (*14, 20*), it is likely that the CO_2(l)/water system is less affected. This is due to the comparatively low surface tension reduction caused by most contaminants in liquid/liquid systems with respect to high σ systems such as gas/water (*14*).

Effects of Oscillation. The effect of oscillations has been demonstrated in a number of bubble experiments in gas/liquid systems and it was shown that the onset of oscillations corresponds to a maximum in u_T and a minimum in C_d (*14*). For methane, it was observed that bubbles released within the methane hydrate stability field changed to a state with reduced shape oscillations and simultaneously, decreased dissolution rates. Both effects have been attributed to the formation of a hydrate skin (*18*). A hydrate skin at the CO_2 droplet surface similarly appears to prohibit oscillations by "freezing in" the shape.

Given the ambiguity in the magnitude of parameters involved, several parameterizations of CO_2 droplet rise velocity are currently used in models describing the fate of

CO_2 droplets rising in seawater (*1, 10, 11*), which are contradictory in theoretical approach and partly rely on different experimental databases (*4, 5*). Applying the velocity theories to the *P*-/*T*-conditions of our experiments, the data of droplets with hydrate at the CO_2/water interface are in excellent agreement with the parameterization of C_d suggested by Chen et al. (*1*) (Figure 4). Neither the approach by Gangstø et al. (*10*) nor the deformation-neglecting approach by Zhang (*11*) are suitable to reproduce our results. The parametrization by Chen et al. (*1*), shows good agreement over the entire range (P, T, r_e) of the data reported by Ozaki et al. (*5*), as well as to the new data set presented here, covering the range of the hydrotherm from roughly 500 to 2000 mbsl. Thus, for droplets in the size range studied here, we strongly suggest the use of the parameterization of u_T developed by Chen et al. (*1*) in models describing the rise of liquid CO_2 droplets for scenarios of midwater CO_2 injection or leakage of CO_2 from subsedimentary storage into the ocean.

3.3. Behavior of Pure Liquid Droplets. The parameterization of Chen et al. (*1*) is valid only if the interface is immobile, which apparently is the case for hydrate-coated droplets. As pointed out earlier, several data points from experiments within the hydrate stability field at pressures ≤11.9 MPa stray from the general trend and the parameterization by Chen et al. (*1*), (Figure 4a−d). Negative deviations from calculated velocities could be correlated with shape oscillations. Our observations suggest that oscillations arose from a lack of rigidifying hydrate at the CO_2/water interface. This might have been due to hydrate nucleii having been shed from the interface at rates higher than the nucleation rate. Hydrate shedding from large CO_2 droplets has been described by Teng and Yamasaki (*21*). Missing hydrate skins also seem to be the reason for higher than predicted velocities at smaller diameters. If hydrate coatings fail to develop in the nonoscillating regime, the surface mobility is left intact and droplets rise faster than their hydrate-covered counterparts. Results of our intercomparison experiments in- and outside the hydrate stability field are shown in Figure 5a−c. The figures show a striking difference between the two sets of data for each $\Delta\rho$, with droplets <5 mm equivalent radius outside the hydrate stability field rising at higher velocities than the majority of the droplets exposed to hydrate-forming conditions. From smallest radii onward Δu_T quickly increased to a maximum at the onset of oscillations. Toward larger radii, velocities of droplets outside the hydrate stability field decreased and ultimately dropped below values measured for droplets inside the hydrate stability field. The curve shapes of the former are typical for droplets and gas bubbles with mobile surfaces and intact internal circulation (*14, 20*). Given the similarity of execution of the experiments, these differences can only be attributed to the ability to form a hydrate skin at the interface. The data therefore not only demonstrate the impact of a hydrate skin on u_T, but also verify (a) that the occurrence of the outliers was caused by a natural effect rather than experimental uncertainty or artifacts and (b) the successful exclusion of surface active contaminants during the measurements.

The similarities of the curve shapes in Figure 5a−c and the outliers in Figure 4a and d strongly support our interpretation that these droplets indeed failed to develop a hydrate skin despite being exposed to hydrate forming conditions. Further evidence is shown in Figure 5b, in which the outlying velocities of droplets exposed to hydrate-forming conditions plot quite well into the curve of data points gained at *P*-/*T*-conditions prohibiting the formation of hydrate. Even though hydrate-coated droplets were observed to be the norm throughout the hydrate stability field as investigated, the observations reveal a growing uncertainty as to hydrate formation the closer pressure and temperature approach the phase boundary. Hydrate skin formation on individual

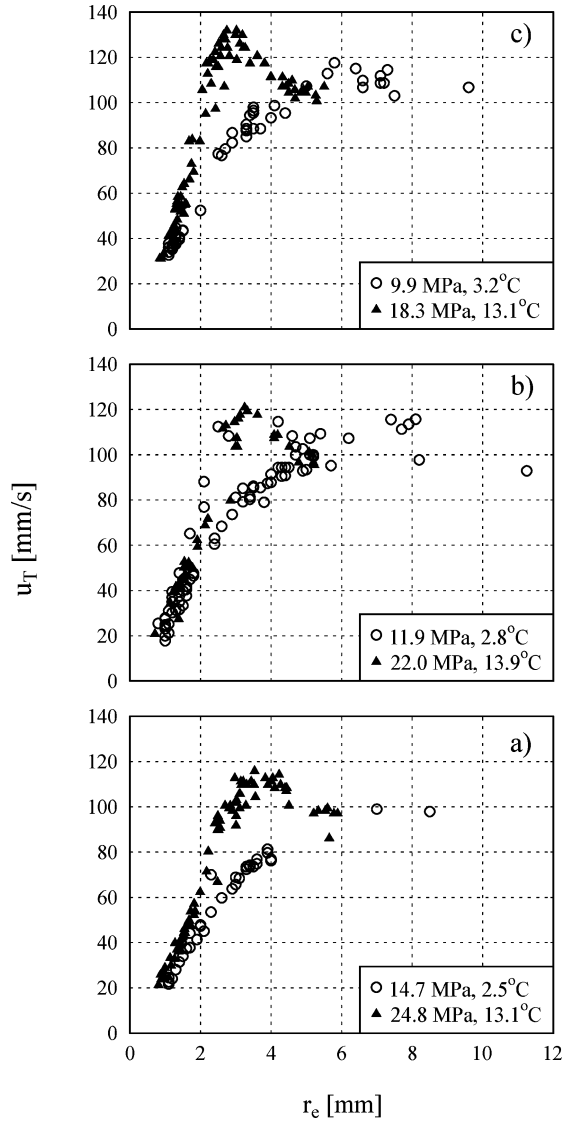

FIGURE 5. Pairs of measured droplet rise rates at *P*-/*T*-conditions inside (circles) and outside (triangles) the field of hydrate stability. $\Delta\rho$ in (a) 47.5 kg/m³, (b) 62.3 kg/m³, and (c) 75.4 kg/m³.

droplets released into a large body of water, such as the real ocean, where background CO_2 concentrations remain low at the point of injection, should be hampered even more than in our laboratory experiments. In the limited volume of water in the experimental chamber (7.9 L), CO_2 concentrations quickly rose during the course of an experiment, though care was taken to maintain the CO_2 concentration far from saturation. Increased CO_2 concentration should decrease the average nucleation time. The situation might be different if leakage of subsedimentarily stored CO_2 occurs. Here, abundant seed crystals in the sediment should facilitate rapid formation of hydrate, as has been observed for the natural CO_2 vents at the NW Eifuku volcano, Mariana Arc, in 1600 m water depth (*22*).

With this work we were able to eliminate any uncertainty concerning the drag parameterization of hydrate covered CO_2 droplets in existing model calculations. To assess the environmental risks involved with large scale release of anthropogenic CO_2 in the deep ocean, we nevertheless recognize the need for further research in this field. Both the effects of droplet dissolution within the field of hydrate stability and the effects of delayed hydrate crystallization have to be addressed experimentally to complement the

existing database currently in use for predicting the fate of droplets rising in oceanic waters.

Acknowledgments

This is publication GEOTECH-323 of the R&D Programme GEOTECHNOLOGIEN funded by the German Federal Ministry of Education and Science (BMBF) and German Research Foundation (DFG), Grant 03G0600D. Furthermore, the work was supported by the European Union within the EU FP6 Integrated Project CARBOOCEAN (Contract 511176). The authors thank two unknown reviewers and Prof. M. Small for their comments on the manuscript. Special thanks go to our technical staff.

Supporting Information Available

Detailed description of the experimental setup and its mode of operation; outline of procedure involving the optical measurement of CO_2 droplets; full data set of aspect ratios of droplets exposed to hydrate forming conditions. This information is available free of charge via the Internet at http://pubs.acs.org.

Literature Cited

(1) Chen, B.; Song, Y.; Nishio, M.; Akai, M. Large-eddy simulation of double-plume formation induced by CO_2 dissolution in the ocean. *Tellus* **2003**, *55B*, 723–730.

(2) Intergovernmental Panel on Climate Change. Special report on carbon dioxide capture and storage; 2005; available at http://www.ipcc.ch/ipccreports/special-reports.htm.

(3) Brewer, P. G.; Chen, B.; Warzinski, R.; Baggeroer, A.; Peltzer, E. T.; Dunk, R. M.; Walz, P. Three-dimensional acoustic monitoring and modeling of a deep-sea CO_2 droplet cloud. *Geophys. Res. Lett.* **2006**, *33*, L23607.

(4) Brewer, P. G.; Peltzer, E. T.; Friederich, G.; Rehder, G. Experimental determination of the fate of rising CO_2 droplets in seawater. *Environ. Sci. Technol.* **2002**, *36*, 5441–5446.

(5) Ozaki, M.; Minamiura, J.; Kitajima, Y.; Mizokami, S.; Takeuchi, K.; Hatakenaka, K. CO_2 ocean sequestration by moving ships. *J. Mar. Sci. Technol.* **2001**, *6*, 51–58.

(6) Radhakrishnan, R.; Demurov, A.; Herzog, H.; Trout, B. L. A consistent and verifiable macroscopic model for the dissolution of liquid CO_2 in water under hydrate forming conditions. *Energy Convers. Manage.* **2003**, *44*, 771–780.

(7) Holder, G. D.; Cugini, A. V.; Warzinski, R. P. Modeling clathrate hydrate formation during carbon dioxide injection into the ocean. *Environ. Sci. Technol.* **1995**, *29*, 276–278.

(8) Hirai, S.; Okazaki, K.; Tabe, Y.; Hijikata, K.; Mori, Y. Dissolution rate of liquid CO_2 in pressurized water flows and the effect of clathrate films. *Energy* **1997**, *22*, 285–293.

(9) Alendal, G.; Drange, H. Two-phase near-field modeling of purposefully released CO_2 in the ocean. *J. Geophys. Res.* **2001**, *106*, 1085–1096.

(10) Gangstø, R.; Haugan, P. M.; Alendal, G. Parameterization of drag and dissolution of rising CO_2 drops in seawater. *Geophys. Res. Lett.* **2005**, *32*, L10612.

(11) Zhang, Y. Fate of rising CO_2 droplets in seawater. *Environ. Sci. Technol.* **2005**, *39*, 7719–7724.

(12) Bozzano, G.; Dente, M. Shape and terminal velocity of single bubble motion: A novel approach. *Comput. Chem. Eng.* **2001**, *25*, 571–576.

(13) Rehder, G.; Steffen, H.; Gust G. Towards investigation of CO_2 phase transition processes using advanced pressure lab technology; UNESCO/SCOR International Science Symposium "The Ocean in a High CO_2 World" Paris, May 10−12, 2004.

(14) Clift, R.; Grace, J. R.; Weber, M. E. *Bubbles, Drops and Particles*; Academic Press: New York, 1978.

(15) Ohmura, R.; Mori, Y. H. Critical conditions for CO_2 hydrate films to rest on submarine CO_2 pond surfaces: A mechanistic study. *Environ. Sci. Technol.* **1998**, *32*, 1120–1127.

(16) Sloan, E. D. J. *Clathrate Hydrates of Natural Gases*, 2nd ed.; Marcel Dekker, Inc.: New York, 1998.

(17) Maini, B. M.; Bishnoi, P. R. Experimental investigation of hydrate formation behaviour of a natural gas bubble in a simulated deep sea environment. *Chem. Eng. Sci.* **1981**, *36*, 183–189.

(18) Rehder, G.; Brewer, P. W.; Peltzer, E. T.; Friederich, G. Enhanced lifetime of methane bubble streams within the deep ocean. *Geophys. Res. Lett.* **2002**, *29*, . doi: 10.1029/2001GL013966.

(19) McGinnis, D. F.; Greinert, J.; Artemov, Y.; Beaubien, S. E.; Wüest, A. Fate of rising methane bubbles in stratified waters: How much methane reaches the atmosphere? *J. Geophys. Res.* **2006**, *111*, doi: 10.1029/2005JC003183.

(20) Leifer, I.; Patro, R. K. The bubble mechanism for methane transport from the shallow sea bed to the surface: A review and sensitivity study. *Cont. Shelf Res.* **2002**, *22*, 2409–2428.

(21) Teng, H.; Yamasaki, A. Hydrate formation on surfaces of buoyant liquid CO_2 drops in a counterflow water tunnel. *Energy Fuels* **1999**, *13*, 624–628.

(22) Lupton, J.; Butterfield, D.; Lilley, M.; Evans, L.; Nakamura, K.; Chadwick, W.; Resing, J.; Embley, R.; Olson, E. Submarine venting of liquid carbon dioxide on a Mariana Arc volcano. *Geochem. Geophys. Geosyst.* **2006**, *7*, . doi: 10.1029/2005GC001152.

(23) Schlitzer, R. Ocean Data View; 2007; available at http://odv.awi.de.

(24) Siedler, G.; Peters, H. Properties of seawater, physical properties (general). In *Landolt-Börnstein-Oceanography; New Series V/3a*; Sündermann, J., Ed.; Springer Verlag: Berlin, 1986.

(25) Angus, S.; Armstrong, B.; de Reuck, K. M. *International Thermodynamic Tables of the Fluid State*; Pergamon Press; Oxford, 1976.

ES800228J